J Mater Sci (2024) 59:12600–12612

Electronic materials

Enhancing electrical properties through in-situ controlled nanocrystallization of V_2O_5–TeO_2 glass

Piotr Okoczuk[1,*], Agnieszka Kwiatkowska[1], Leon Murawski[1], Tomasz K. Pietrzak[2], Natalia A. Wójcik[1], Fabian Garmroudi[3], Leszek Wicikowski[1], and Barbara Kościelska[1]

[1] *Institute of Nanotechnology and Materials Engineering, Gdansk University of Technology, Narutowicza 11/12, 80-233 Gdansk, Poland*
[2] *Faculty of Physics, Warsaw University of Technology, Koszykowa 75, 00-662 Warsaw, Poland*
[3] *Institute of Solid State Physics, TU Wien, 1040 Vienna, Austria*

Received: 27 March 2024
Accepted: 27 June 2024
Published online: 7 July 2024

ABSTRACT

V_2O_5–TeO_2 glass–ceramics (VTGC) were prepared by controlled annealing of the V_2O_5–TeO_2 glass (VTG), which illustrates a parent glass matrix with a single charge carrier. The annealing proceeded at six temperatures selected between the glass transition and the maximum of the first crystallization process to obtain various nanocrystallite sizes. Heat treatment caused an increase in DC conductivity by 2.5–3.5 (250–285 °C) order of magnitude. Using thermal analysis, the crystal growth process was determined to be 1D. Structural studies show that the obtained materials are partially amorphous and polycrystalline with nanometer-sized crystallites. Subtle thread-like structures were observed using conductive AFM. The activation energy of the conduction process decreased from 0.38 eV in VTG to 0.18–0.11 eV (250–285 °C) in VTGC. The radii of crystallites were calculated based on the theoretical model of electron hopping between connected semiconducting nanocrystallites and vary between 1.7 and 2.8 nm (250–285 °C). Thermoelectric studies indicate constant carrier concentration. Features characteristic of small polaron hopping-governed materials were observed. We suggest V_3O_7 nanocrystals as conductive media in VTGC.

Handling Editor: Till Froemling.

Address correspondence to E-mail: piotr.okoczuk@pg.edu.pl

https://doi.org/10.1007/s10853-024-09957-y

GRAPHICAL ABSTRACT

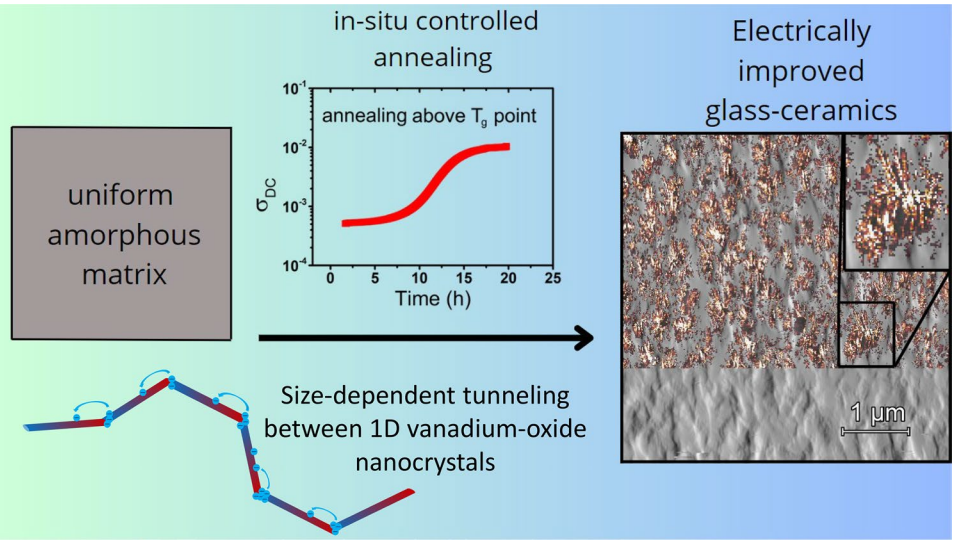

Introduction

Like many transition metal oxide (TMO) glasses, V_2O_5–TeO_2 glass (VTG) is an interesting material due to its unique semiconducting properties and applications, for example, electrical and optical memory switching, cathode and anode materials, and so on [1–3]. However, the electrical conductivity of VTG is relatively low (10^{-6} S/cm at room temperature), which limits its practical applications in the field of materials for energy storage. Vanadium-oxide-containing glass–ceramics (VOGC) may be competitive candidates as the VTG's crystallization can increase electrical conductivity by 2.5–3.5 orders of magnitude at room temperature, which was first recognized in late 70′ [4]. However, it has not yet been clearly explained how the conduction mechanism changes during the gradual heating of this glass. Understanding charge transport in glass–ceramics will give the ability to control and design their properties for developing advanced electronic and optoelectronic devices.

Small polaron creation and hopping between ions with different valence states, such as V^{4+} and V^{5+}, play a crucial role in the electrical conductivity of TMO glass and have been previously considered as possible charge transfer mechanism in VOGC [5]. Research conducted by Garbarczyk et al. significantly contributed to understanding the electrical conductivity process in glass–ceramics [6–10]. Their studies of the structural, electrical, and thermal properties of V_2O_5–P_2O_5, Li_2O–FeO–V_2O_5–P_2O_5, and $Na_3V_2(PO_4)_2F_3$ (NASICON-like) glasses suggest that, in most of the systems, a disordered shell of nanocrystallites contains a higher concentration of V^{4+} ions, thus preserving the polaronic nature of electrical conductivity.

Our previous study of direct current (DC) conductivity of V_2O_5–TeO_2 glass–ceramics (VTGC) also showed the applicability of the small polaron hopping (SPH) model, employing the Schnakenberg polaron hopping model and Triberis-Friedman percolative SPH [5]. However, such low activation energies as ~ 0.1 eV present in VTGC are not usual in SPH charge transfer, and none of the vanadium oxide allotropes has yet been addressed as directly responsible for such high conductivity in the VOGC.

Thermal annealing of the glass above the glass transition temperature (T_g) strongly affects its structure. In multiple glass compositions, it was shown that thermal treatment results in the presence of nanocrystals (NC) with a radius of a few nanometers, showing its direct influence on the conductivity of the resulting glass–ceramics [11, 12]. When NCs are metallic, the charge transfer mechanism was often recognized as electron tunneling between metallic nano-sized crystals. Shklovski et al. showed that the charge transfer between connected semiconducting NCs can occur in a similar manner [13, 14]. The energy (E) required to load such NC would be expressed by the formula [13]:

$$E = \frac{e^2}{2C} = \frac{e^2}{8\pi\varepsilon_f\varepsilon_0 r} \quad (1)$$

, where C is the capacitance of an NC immersed in the array, e is an electron charge, ε_f is an effective permittivity, ε_0 is a permittivity of free space, and r is the nanocrystal radius. E should be equal to the activation energy of the conduction process. V_2O_5–TeO_2 glass–ceramics exhibit nanocrystalline structure [5], therefore it is essential to also consider the charge transfer between connected semiconducting NC.

To properly understand the process of nucleation and growth of the crystallites, the Johnson–Mehl–Avrami (JMA) [15–17] formula can be used to study the isothermal differential scanning calorimetry (iso-DSC) results. The dimensionality of the isothermal crystallization process can be analyzed using established theoretical models. The time dependence of the volume fraction of the crystalline phase during isothermal crystallization can be described in the JMA equation as follows:

$$Y(t) = 1 - \exp\left(-K\left(t - t_0\right)^n\right) \quad (2)$$

, where n is the exponent related to the dimensionality of the crystallization process [18], K is the constant depending on the crystallization rate, and t_0 is the time of the start of the crystallization.

In line with the kinetic viewpoint on glass formation, when glass is annealed at temperatures sufficiently close to the T_g, the progression to crystal growth can be impaired, focusing solely on the nucleation process. The NC's concentration and dimensions can be governed by controlling the glass annealing temperature. Given, that the activation energy should be contingent on the crystallite size (Eq. 1), this study presents a comparative analysis of samples heat-treated at different temperatures.

While, numerous papers exist on variously doped V_2O_5–TeO_2 glass [19–21], the discussion about the crystallization mechanism and its influence on the charge transport mechanism in this system has often been neglected. An example are the works in which VTGC systems were doped with lithium and were characterized by superior ionic conductivity [21, 22]. A deep understanding of the charge transport evolution during the crystallization of the exemplary glass matrix appears crucial for delineating the direction of further studies. Our previous work extensively examined various charge transport models typically considered in glass and glass–ceramics to identify the dominating charge transfer [5]. We also studied different glass compositions to observe the correlation between changes in vanadium oxide content and the controlled crystallization process, as well as their influence on the electrical conductivity of glass. In contrast, the current study focuses on nucleation processes and well-controlled nuclei growth in the 50 mol% V_2O_5– 50 mol% TeO_2 glass, which exhibited the highest electrical conductivity among those previously tested. Here, the nanocrystallization process is analyzed regarding thermal and morphological properties. For the first time, the combination of iso-DSC and C-AFM techniques is used to illustrate the structural distribution of conductive paths and support electrical information. This approach allows us to discern differences in conductive properties based on the changes in nanocrystal size. By integrating these complementary analyses, we evaluated the electrical properties by fitting a theoretical model of electron tunneling between connected semiconducting nanocrystals [13], to assess the size of the structures responsible for charge transfer. Proposed charge transport fits well with the data and should also be recognized as a probable approach for understanding the creation of conduction paths in vanadium-oxide-containing glass–ceramics.

Experimental

VTG with composition of 50 mol%–50 mol% was prepared using V_2O_5 (Acros Organics, 99.6 + %) and TeO_2 (Acros Organics, 99 + %). Powders were mixed in the agate mortar. Batches of 15 g of mixed powders were melted in the furnace in the silica crucibles (covered with a silica plate) at 800 °C for 30 min. The melt was poured on the cold steel plate and pressed with another steel plate, resulting in samples within ~ 1 mm thick. Obtained glass samples were annealed at 110 °C for 10 h to release the internal stress in the glass. The annealing temperature was intentionally significantly lowered relative to T_g to avoid accidental nucleation. However, the extended annealing time was sufficient for the samples to become stable and suitable for mechanical processing. Glass sample amorphousness and homogeneity were proven and shown in Supplementary Fig. S1 online. Then, the samples were subjected to crystallization controlled by monitoring the DC resistance of the heat-treated samples. Six temperatures of the crystallization process were

chosen based on the results obtained from DSC tests. As a decrease in resistance was observed during the crystallization process, the crystallization time was determined as the resistance reached a stabilization point, after which samples were cooled down. Samples subjected to crystallization upon DC resistance monitoring were named according to Table 1 and later studied structurally.

Thermal events occurring in the glass material were observed with a TA Q200 DSC instrument on the powdered glass samples. Initially, DSC scans were carried out in a non-isothermal mode from 40 to 450 °C, with a heating rate of 10 °C/min. The objective was to examine the thermal characteristics of the prepared glass and identify the appropriate temperatures for subsequent experiments such as isothermal annealing and iso-DSC. During iso-DSC studies of the glass, the sample was rapidly heated to the set point temperature (within the 265–285 °C range). The duration of this stage was ca. 2 min, providing an average heating rate of 100 °C/min. Subsequently, the temperature of the sample was immediately stabilized at the set point, and the acquisition of the isothermal DSC signal began.

For the isothermal annealing upon in-situ DC resistance monitoring, samples were polished with sandpaper to the thickness l ~ 0.5 mm to obtain a smooth sample surface. For the electrical measurements, gold electrodes with a diameter of ~ 0.8 cm were sputtered on the surface of the samples (images of samples and measurement cell shown in Supplementary Fig. S2 online). The resistance of the samples was measured by a two-wire method using a Keysight 34907A multimeter with data acquisition. Based on previous studies, this configuration show no additional electrode effects during the measurements. Additionally, it was shown that conductivity of studied glass–ceramics is frequency-independent at high temperatures [5]. To calculate the conductivity of the sample, the dependence $\sigma = l/(R \cdot A)$ (where σ is the conductivity of the sample, R is the measured resistance, and A is the area of the electrode) was used. Crystallization of the samples was done in an air atmosphere. All electrical measurements and fitting results are affected by a measurement error not exceeding 4%.

Table 1 Sample identification table

Annealing temperature (°C)	Sample name	Time of annealing to obtain maximum DC conductivity
250	250C	310 h
265	265C	57 h
270	270C	52 h
275	275C	28 h
280	280C	18 h 10 min
285	285C	8 h 10 min

The structure of as-quenched and heat-treated samples was examined by XRD using an X'Pert Phillips diffractometer with Cu Kα radiation (1.541 Å). The XRD measurements were carried out on the powdered samples at room temperature. The diffraction patterns of crystallized samples were analyzed using the HighScorePlus software package.

FTIR analysis in the 4000–400 cm^{-1} IR region was carried out using the Spectrum 2 Perkin Elmer spectrometer in the reflective mode with the diamond detector on powdered samples.

Atomic force microscopy (AFM) and conductive atomic force microscopy (C-AFM) in contact mode were used to study the surface of the sample intersections. The microstructure and electrical properties of all samples were charted using AFM at their fresh fractures using NT-MDT Ntegra AFM. Different probes were utilized to analyze topographical and conductive properties to obtain a better resolution of the resulting image.

Low-temperature investigations (230–300 K) of the electrical resistivity and Seebeck coefficient have been performed at an in-house setup. The resistivity was measured using a four-probe method with an AC resistance bridge (Lakeshore) and an excitation current of 31.6 mA. Thin gold wires were sputtered onto the sample surface in the appropriate geometry, and the sample was mounted in a Helium bath cryostat. The low-temperature Seebeck coefficient was measured using a toggled heating technique with two constantan–chromel thermocouples that were thermally contacted to the sample.

Results and discussion

Thermal analysis and crystallization

In the DSC curve (Fig. 1a), endothermic drift, characteristic of amorphous materials, can be seen, which corresponds to the glass transition (T_g). After the glass transition point, several exothermic processes related to crystallization take place. The

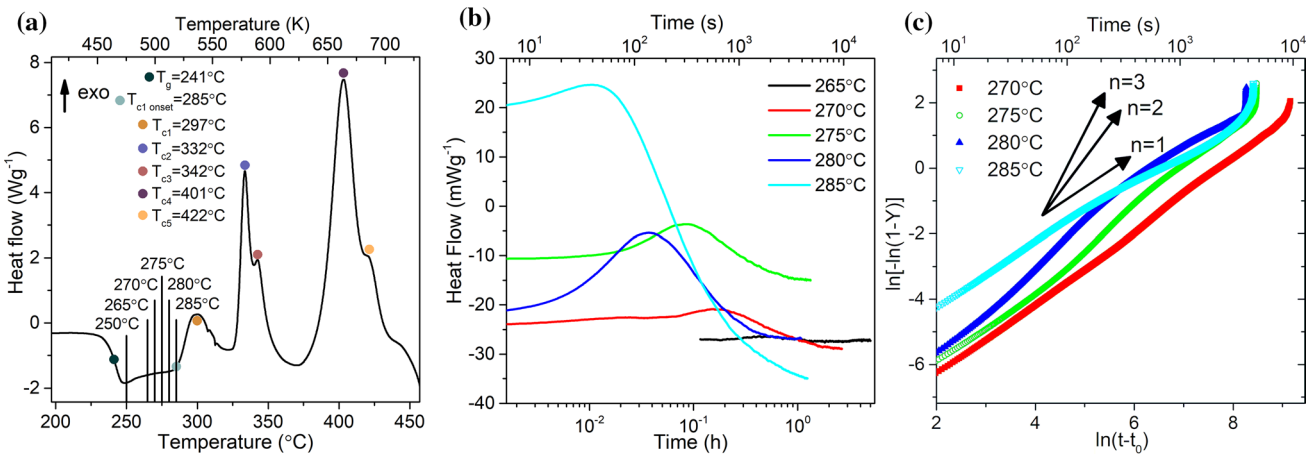

Figure 1 **a** DSC curve of parent $50V_2O_5$–$50TeO_2$ glass (in %mol). The chosen crystallization temperatures and characteristic temperatures are identified in the plot. Characteristic temperatures are also listed. **b** Time dependence of the DSC signal during isothermal glass annealing at pre-selected temperatures. **c** Time dependence of the crystalline fraction $Y(t)$ shown in $\ln[-\ln(1-Y)]$ coordinates with arrows drawn to visualize the dimensionality of the crystallization process according to the JMA formula.

temperatures associated with the maximum of the crystallization peak (T_{cx}), where x is the number of peak, are shown in the Fig. 1a. Glass thermal stability (S) was calculated using: $S = T_{c1\ onset} - T_g$ and is equal $S = 44$ °C [23]. To eliminate the nucleation and growth of as many crystalline phases as possible, constrain growth, and focus on the nucleation and of the nanocrystalline phase with the lowest crystallization temperature, six crystallization temperatures between Tg and T_{c1} were selected for the annealing upon DC resistance monitoring: 250, 265, 270, 275, 280, and 285 °C. According to the ref. [24] in similar glass, the first thermal event in the thermogram can be recognized as a sign of nucleation. In Fig. 1b, iso-DSC scans are shown, demonstrating that the nucleation rate also accelerates as the temperature of the experiment increases. Only thermograms of samples annealed at 275 °C and 280 °C show a distinctive start and the end of the nucleation process.

The DSC signal observed during the crystallization process at 265 °C is meager, and as such, it will not be subjected to further investigation for iso-DSC models. Thermograms for the other crystallization temperatures show only one crystallization maximum within the first 10,000 s of crystallization.

From the iso-DSC scans, the time dependence of the volume fraction of the crystallized material $Y(t)$ can be calculated. As it corresponds to a part of the entire area under the crystallization maximum at a specific time of crystallization, it can also be written as:

$$Y(t) = \int_{t_0}^{t} H(t)dt \Big/ \int_{t_0}^{t_f} H(t)dt \tag{3}$$

, where $H(t)$ is the heat flow at time t, and t_0 and t_f are the times of the beginning and the end of the observable crystallization. By combining experimental results with Eq. (2) and utilizing linear fitting, one can derive parameters n and K.

This can be achieved by plotting the data in the form of $\ln\left[-\ln(1-Y(t))\right]$ versus $\ln(t-t_0)$ plot. In Fig. 1c, it can be seen that for analyzed crystallization temperatures, the conducted process is one-dimensional (1D). The slight nonlinearity of the n parameter at the beginning of the crystallization at the temperatures of 275 °C and 280 °C may indicate the presence of an inhomogeneous distribution of crystal nuclei in the glass matrix before crystallization [25]. The best-fit

Table 2 n and K parameters obtained from fitting of Eq. (2) to data in Fig. 1c

Temperature of the experiment	270 °C	275 °C	280 °C	285 °C
n (±0.1%)	1.12	1.19	1.04	0.84
K (±0.1%)	−8.66	−8.31	−6.71	−5.52

parameters of n and K for the respective temperature are shown in Table 2. To relate the iso-DSC results with the increase in conductivity, the crystallization process of glass samples upon the monitoring of DC resistivity was performed. The results were calculated to conductivity versus time and temperature dependence (Fig. 2a–d). During the heating, the electrical conductivity increased by ~1.5 orders of magnitude (Fig. 2d). The higher the annealing temperature, the higher the increase in conductivity. The crystallization time necessary to obtain the maximum possible conductivity was determined to be 310 h, 57 h, 52 h, 28 h, 18 h 10 min, and 8 h 10 min for temperatures of 250, 265, 270, 275, 280, and 285 °C, respectively. A heat-treated sample will be later called "250C" for the temperature of annealing 250 °C, "265C" for the temperature of annealing 265 °C, and so forth. As can be seen, the crystallization time decreases as the temperature of the crystallization process increases. Moreover, the crystallization time at all temperatures estimated from conductivity measurements significantly exceeded the time of crystallization obtained from iso-DSC (Fig. 1), which was observed before in similar glass [24], meaning that the observed thermal event corresponds to the nucleation process. To determine the dimensionality of the subsequent crystallization process, extended iso-DSC measurements were conducted for annealing temperatures of 275 °C and 280 °C due to observation of the entire crystallization maximum on short iso-DSC thermograms (Fig. 1b). The crystallization process monitored by DC resistivity was compared with extended iso-DSC in Fig. 2a, b. As shown in Fig. 2a–c, another crystallization maximum can be found after the first. At the temperature of crystallization of 275 °C (Fig. 2a), three main crystallization maxima can be distinguished (Fig. 2a) (red lines were drawn to guide the eye). It should be noted that the time of the end of the second crystallization maximum corresponds to the time of crystallization determined using the DC conductivity measurements. For the crystallization temperature of 280 °C, prolonged crystallization shows multiple crystallization maxima. Figure 2c

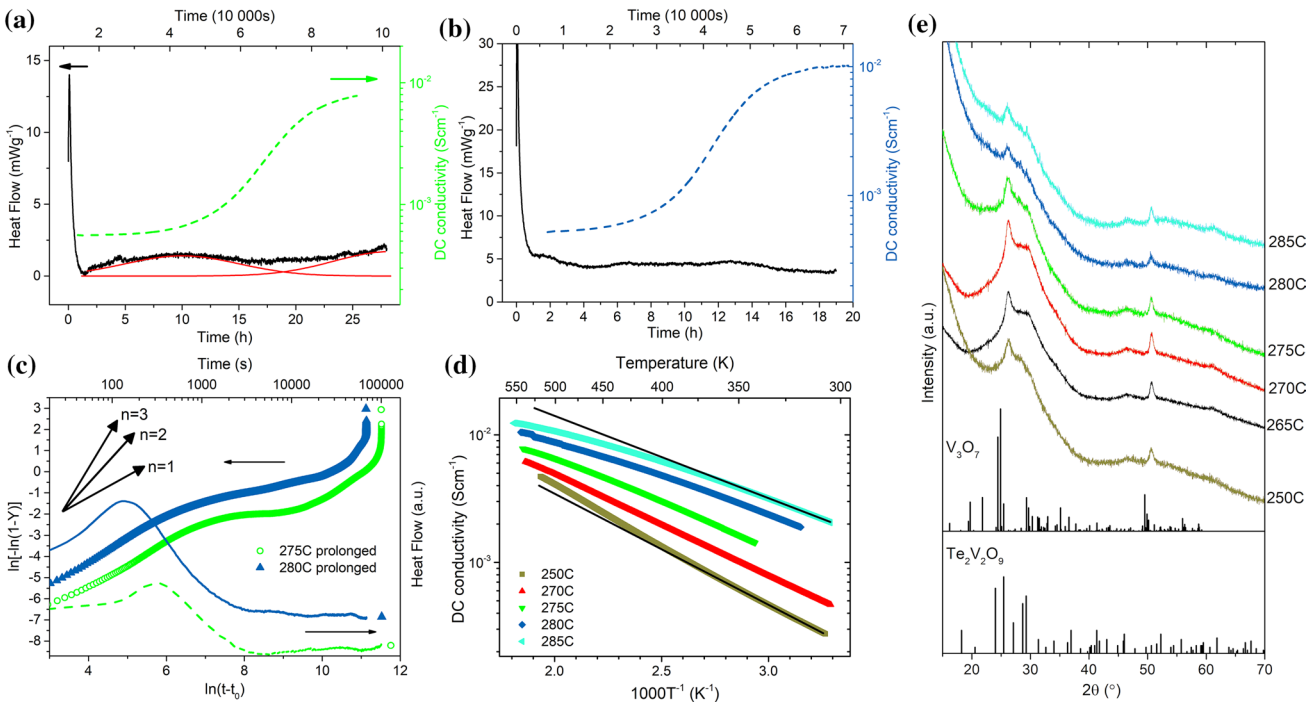

Figure 2 **a** Heat-flow and conductivity versus time during the prolonged isothermal crystallization of glass sample at 275 °C, **b** Heat-flow and conductivity versus time during the prolonged isothermal crystallization of glass sample at 280 °C and **c** Time dependence of crystalline fraction plotted in $\ln[-\ln(1-Y)]$ versus $\ln(t-t_0)$ coordinates plotted along with heat flow during the isothermal crystallization. For easier data interpretation, arrows were drawn to visualize the dimensionality of the crystallization process according to the JMA formula **d** conductivity versus. Inverse temperature plot of isothermal annealing of glass at various temperatures upon DC conductivity monitoring. **e** X-ray diffractograms of glass–ceramics with standard patterns of crystalline V_3O_7 and $Te_2V_2O_9$.

shows that the intensity of heat flow is very low for subsequent crystallization maxima. According to the JMA formula, the prolonged crystallization process exhibits a similar dimensionality to the first crystallization maximum (1D).

Structure

The structure of obtained glass and glass–ceramics was studied by XRD and shown in Fig. 2e. A broad bump around 20°–30° is observed for the parent glass, a characteristic amorphous material. In glass–ceramics, the diffractogram shows two broad reflections at 26° and 51°. Based on the reflections' width, it can be estimated that the size of the observed crystallites is lower than 20 nm [26]. At high and low crystallization temperatures, the intensity of the amorphous halo at low angles (15–25°) increases, which can be associated with an increased presence of nanostructures in samples 250C, 275C, 280C, and 285C. Because of the small crystalline size and broad diffraction reflections, phase identification can be made with considerable uncertainty. However, Bragg angles of two distinct reflections fit well with the V_3O_7 pattern (ICDD 01–071–0454) (Fig. 2e), which crystallizes in the monoclinic structure with C2/c symmetry. In earlier work [5], the $Te_2V_2O_9$ (ICDD 00–018–1330) phase was observed during the crystallization at the temperature of the first crystalline maximum, which fit well to the obtained spectra despite the presence of a reflection at the angle of 24° present in the standard pattern (Fig. 2e). According to the DSC curve (Fig. 1a), both crystalline phases may coincide.

The glass and glass–ceramics FTIR spectra (Fig. 3) revealed characteristic absorption bands corresponding to various bond types. The absorption band corresponding to VO_2 groups was observed in all samples and shifted after crystallization from 970 to 980 cm^{-1} [27]. This shift suggests a shortening of the bond between vanadium and oxygen atoms. This can also be seen in the accompanying increase in the intensity of the 500 cm^{-1} band, indicating the presence of VO_2 groups. Crystallization of the glass (except the 250C sample) also resulted in an appearance of the band at 1020 cm^{-1}, indicating the presence of VO_5 groups in a crystalline structure of V_2O_5 [28]. Furthermore, in the samples 285C and 280C, the absorption band corresponding to TeO_4 groups shifted from 620 to 650 cm^{-1}, indicating an increment of the TeO_3 groups [29, 30]. Confocal microscopy studies were performed

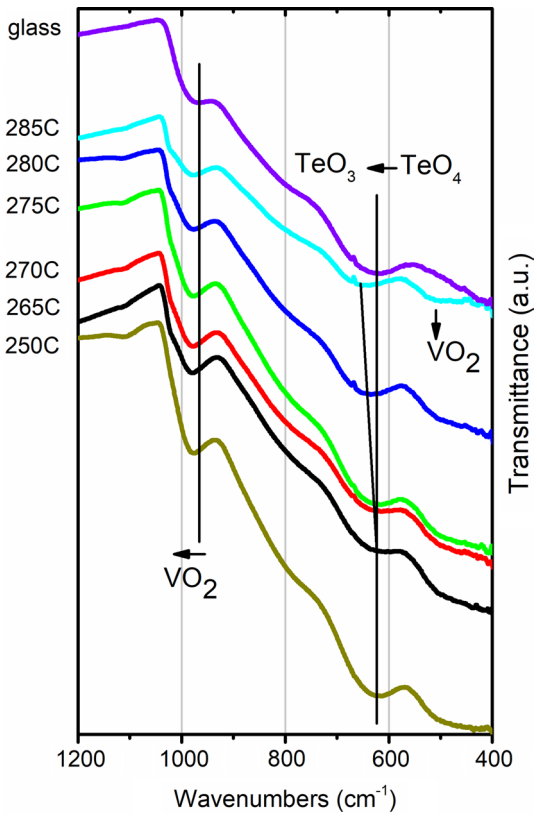

Figure 3 FTIR spectra of all samples with black straight lines drawn to guide the eye.

to investigate the topography of sample intersections on a micro-scale (Fig. 4). The glass sample exhibits no repeatable structure, confirming the amorphousness. A comparison of 3D profiles shows granulation of the glass upon annealing at higher temperatures.

AFM microscopy was used to observe the topography of fresh-fractured samples at a nanoscopic scale. DFL images shown in Fig. 5 show a gradual increase in the mean granule size with an increase in the annealing temperature up to 270 °C. XRD studies do not indicate the presence of crystals bigger than 20 nm, which suggests that observed agglomerates have a nanocrystalline/amorphous nature. The grain sizes observed at the fracture of sample 275C do not show any further increase and are more random. For samples 280C and 285C, the fracture surface exhibits larger agglomerates of grains. Three height profiles were drawn at each image, as shown in Fig. 5 and shown in Supplementary Fig. S3 online. From each high profile, granule sizes were estimated by measuring the granule height (as in Supplementary Fig. S3(f) online). Granule sizes are shown in Supplementary

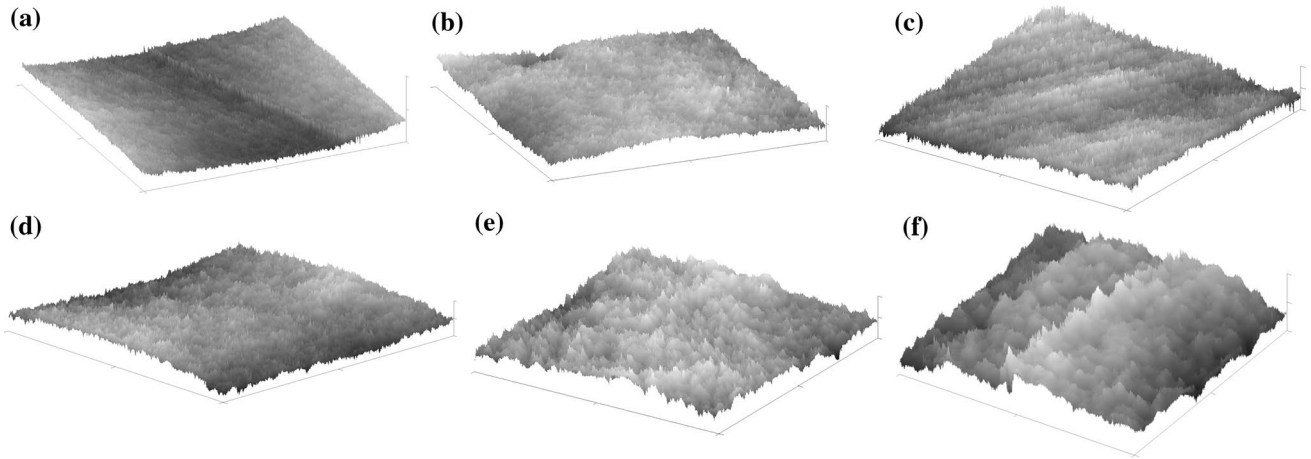

Figure 4 3D visualization of the fracture surface of samples **a** 250C, **b** 265C, **c** 270C, **d** 275C, **e** 280C, and **f** 285C from the high profile of confocal images. The edge of a presented profile is equal to 130 µm.

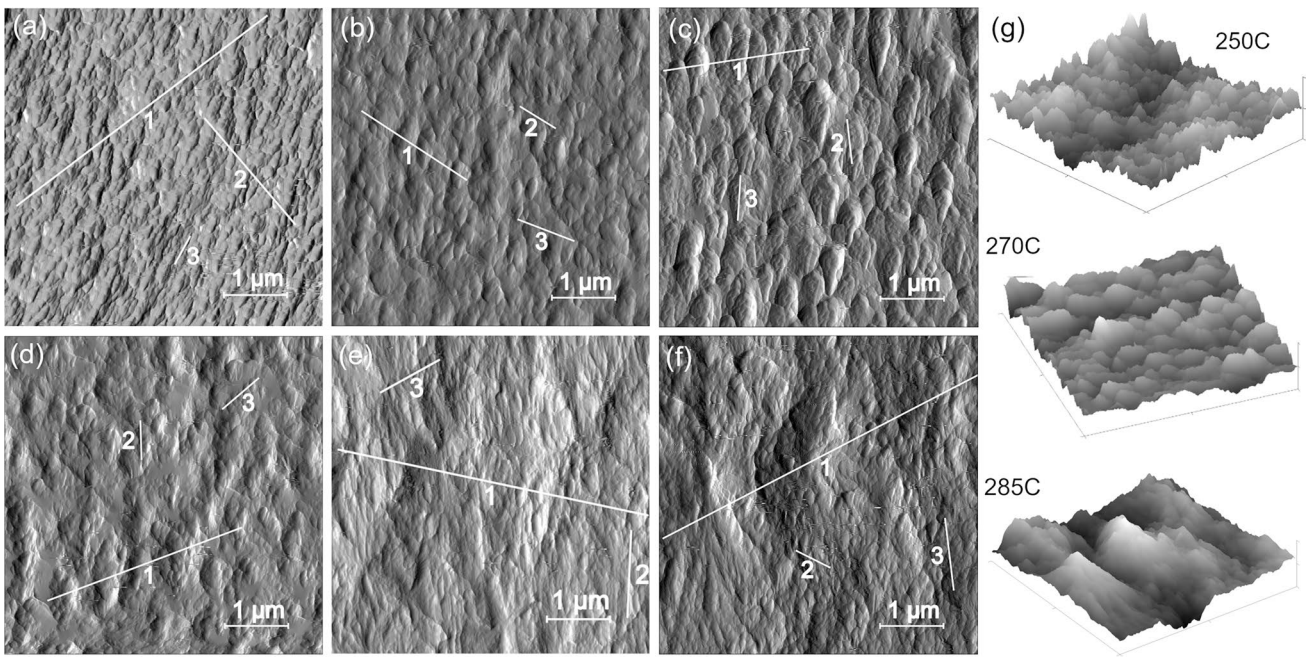

Figure 5 AFM DFL images of samples: **a** 250C, **b** 265C, **c** 270C, **d** 275C, **e** 280C, and **f** 285C with marked height profiles and scale. **g** 3D projection of high profile of samples 250C, 270C, and 285C.

Table S1 online. In samples 250C, 265C, and 270C, small granules (1–200 nm) dominate and can be seen on relatively flat surfaces; no larger agglomerates can be noticed. Increasing the annealing temperature above 275 °C (275C, 280C, and 285C) results in a more rippled surface with bigger agglomerates (~ 300, ~ 400, and ~ 500 nm, respectively) on which smaller granules with a size of a few nanometers (~ 10, ~ 8, and ~ 5 nm) can also be recognized. The partially amorphous nature of the glass–ceramics observed using AFM agrees with the XRD results. The change in the granulation of the matrix appears to be correlated with the reorganization of TeO_4 trigonal bipyramids into TeO_3 trigonal pyramids observed in FTIR spectra of samples 280C and 285C (Fig. 3).

DFL images were used to overlay C-AFM images during the acquisition of conductivity imaging, as shown in Fig. 6. The less conductive regions of the

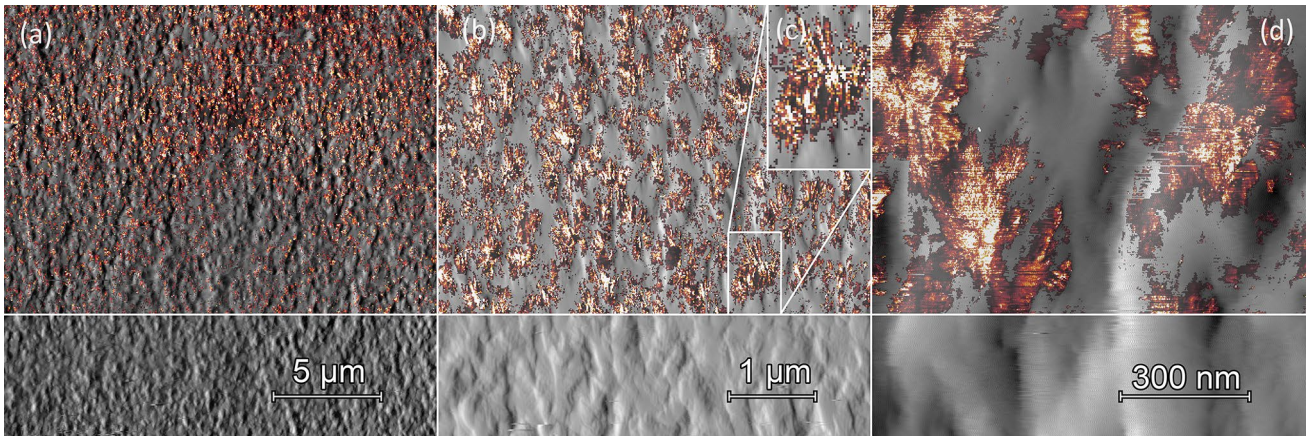

Figure 6 DFL images with C-AFM images overlayed to highlight the placement of better conductive areas. Orange-to-white regions correspond to the better conductive areas. All images correspond to different magnification rates of sample 270C, where the edge of an image is equal to **a** 20 µm, **b** 5 µm, and **d** 1 µm. The inset **c** shows that thread-like structure areas exhibit higher conductivity.

C-AFM image were removed from the image. The orange to white areas represent more conductive regions, whereas the white areas indicate the most conductive ones. In Fig. 6b, c, one can notice that the better conductive structures exhibit dendritic/thread-like shaped structures. No repeatable structures can be observed even for the highest magnifications (Fig. 6d). Both of the above-mentioned features support the 1D crystal growth observed in the iso-DSC. Additionally, the dendritic/thread-like shape of crystal growth is widely known in the vanadium oxides of low oxidation states. Consolidating the C-AFM and the topographical images, one can also notice that more rippled surfaces are more likely to show higher conductivity than flat areas (Fig. 6b, d).

Transport properties

The effect of heat treatment on the electrical properties of VTG was also studied. Figure 2d shows the changes in the conductivity upon annealing at all applied temperatures. The maximum conductivity of nanocrystalline VTGC studied in this work reached $9*10^{-3}$ S/cm at room temperature for the sample 285C, which is comparable to the conductivity of nanocrystallized $90V_2O_5$–$10P_2O_5$ (in %mol) glass–ceramics [7] and higher than observed glass–ceramics with lower vanadium oxide content [5, 31].

Time dependency of conductivity increase shows a sigmoid shape (Fig. 2a, b). When obtaining the highest possible DC conductivity, samples annealed at higher temperatures exhibited higher electrical conductivity.

To evaluate the activation energy of the conduction process (W), the Arrhenius-type equation was used, in which the temperature dependence of conductivity can be expressed as:

$$\sigma = \sigma_0 \exp\left(-\frac{W}{kT}\right), \tag{4}$$

, where σ_0 is a pre-exponential factor, k is the Boltzmann constant, and T is the absolute temperature. Equation (4) was fitted to the conductivity dependence shown in Fig. 2d to estimate the activation energy of the conductivity process. The fitting results are shown in Table 3. Linear fit of the heating curve of

Table 3 Activation energy of the conduction process obtained from the fitting of Eq. (4), range of the activation energy W, and crystal size calculated from Eq. (1)

Sample name	Activation energy W from linear fitting (eV)	Activation energy W variation (eV)	Crystal size 2r (nm)
Glass	0.38	±0.10	–
250C	0.18	±0.01	1.7
265C	–	–	–
270C	0.16	±0.01	1.9
275C	0.14	±0.04	2.2
280C	0.12	±0.05	2.5
285C	0.11	±0.05	2.8

the crystallization process was used to estimate W of the glass to be ~ 0.38 eV, which is a similar value to observed previously in this glass [32]. After crystallization, linear fitting of cooling curves shows that W varies with the annealing temperature from 0.18 to 0.11 eV (250C–285C). Using the activation energy and Eq. (1) one can obtain the nanocrystal size ($2r$) between which charge transfer occurs in the model of electron tunneling between connected semiconducting crystals. Calculated nanocrystal sizes show an increase in the crystal size from 1.7 nm for the 250C sample to 2.8 nm for the 285C sample.

The separated cooling parts of the DC studies are shown in Fig. 7a. The plot of conductivity versus inverse temperature indicates that the Arrhenius behavior is not entirely followed, especially for fringe temperatures of sample annealing. This is evident from the black lines drawn on the plot to aid visualization. According to Eq. (1), the electrical conduction process between connected nanocrystals should exhibit constant activation energy, known in Arrhenius behavior. This suggests that our glass–ceramics involve a second charge transfer process. To determine the relationship between activation energy and temperature dependence, one can analyze the derivative of $\ln\sigma(T)$ over $1/T$, which should be equal to the negative value of activation energy (W):

$$W(T) = -\frac{\partial \ln\sigma(T)}{\partial \frac{1}{T}}. \tag{5}$$

Figure 7b illustrates the relationship between activation energy and temperature, revealing that only the 270C sample exhibits consistent activation energy in a wide temperature spectrum. The W value of samples subjected to higher annealing temperatures decreases as the temperature rises.

This trend is comparable to that observed in crystalline V_2O_5 at a similar temperature range, attributed to electronic transport via free carrier flow [33]. Based on previous research on low-temperature conductivity of this material [5], the decline in W with decreasing temperature in the 250C sample can be recognized as a feature of SPH. Mott [34] showed that for SPH activation energy (W) should decrease with decreasing temperature at temperatures below $\theta_{OP}/4$ (where, $\theta_{OP} = h\nu_{OP}$, and ν_{OP} is the optical frequency correlated with SPH process [5]) stable between $\theta_{OP}/2 < T < \theta_{OP}/4$, but increase with increasing temperature above $\theta_{OP}/2$ [33]. This observation, in agreement with previous studies [5], shows that higher annealing temperature leads to a more significant decrease of ν_{OP}. The V_6O_{13} compound displayed comparable activation energies of the conduction process [35, 36], which can be attributed to its V^{4+}/V^{5+} ratio (a crucial factor for SPH) being similar to that of the V_3O_7 compound.

Thermoelectrical studies of the 285C sample were shown in Fig. 7c. Seebeck coefficient remains constant in the measured temperature range. This can be interpreted as a constant carrier concentration, which can be seen in the case of hopping charge transport mechanism [37–39]. This result supports both SPH and hopping between semiconducting nanocrystals. Changes in the activation temperature (Fig. 7b) are much less significant than observed previously in glasses in which SPH governs the charge transfer [5, 40, 41]. The possible presence of hopping between semiconducting

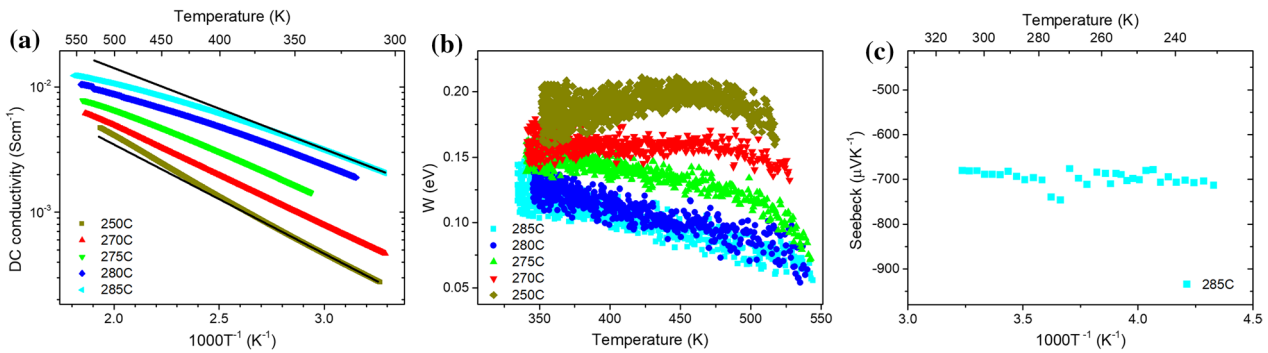

Figure 7 **a** Conductivity versus 1000 T^{-1} for the glass–ceramics after annealing at the specific temperature shown in the legend. Black lines guide the eye and follow the Arrhenius formula, **b** W versus T plot calculated using Eq. (5), **c** Seebeck coefficient of the 285C sample.

nanocrystals cannot be neglected and may be involved in the charge transfer process in VTGC.

Conclusions

In this work, we presented a combination of a few techniques to perform controlled nanocrystallization of the V_2O_5–TeO_2 glass. First, we employed a classical thermal analysis to obtain a set of temperatures necessary to analyze crystallization in the nanoscale. Then, the iso-DSC of powdered glass was used to study the nucleation and growth of crystallites at the selected temperatures and was determined to be 1D. Thirdly, the annealing time upon DC resistance observation was specified to obtain the maximum possible electrical conductivity of glass–ceramics. Samples that underwent annealing at various temperatures were later studied regarding structural properties. Based on XRD, it was concluded that the obtained material consist of an amorphous phase and nanometer-sized crystallites. Two observed maxima in the diffractogram suggest the presence of the V_3O_7 phase. FTIR analysis showed an increase in VO_2 band intensity after crystallization and TeO_4 group reorganization at high annealing temperatures. By AFM and C-AFM methods, it was recognized that restraining crystal growth was accomplished. The results support the 1D character of crystallite growth and show its influence on conducting properties. The DC conductivity temperature dependence obtained during the annealing showed that W dropped from ~ 0.38 eV in glass to 0.18–0.11 eV (250C–285C) in glass–ceramics. The applicability of the theoretical model of electron tunneling between connected semiconducting nanocrystals was confirmed. The calculated radius of the crystallites between which charge transfer occurs varies with the temperature from 1.7 to 2.8 nm (250C–285C). The temperature dependence of W and thermoelectric analysis showed characteristic features of SPH, which may be the second charge transfer in the investigated system. Finally, we suggest that the conductive media in V_2O_5–TeO_2 glass–ceramics are connected chains of 1D V_3O_7 nanocrystallites, inside which SPH governs charge transfer. Charge accumulation is a major problem in similar electrode materials. Improving the charge transport properties by creating highly conductive vanadium-oxide one-dimensional percolation paths may significantly impact the development of new, both electrically and ionically well-conducting materials.

Acknowledgements

Piotr Okoczuk wishes to thank Dr. Marta Roman and Prof. Herwig Michor for the discussion about the thermoelectric properties of our materials.

Author contributions

P.O.: Conceptualization, Methodology, Investigation, Formal Analysis, Data Curation, Writing–Original Draft; Writing–Review and Editing; A.K.: Methodology; L.M.: Conceptualization, Investigation; T.P.: Methodology, Validation; N.A.W.: Writing–Review and Editing; F.G.: Methodology; L.W.: Conceptualization; B.K.: Supervision, Validation, Conceptualization, Resources.

Data availability

The data presented in this study are openly available at: https://mostwiedzy.pl/pl/piotr-okoczuk,1038332-1/research-data.

Declarations

Conflict of interest The authors declare no competing interests.

Supplementary Information The online version contains supplementary material available at https://doi.org/10.1007/s10853-024-09957-y.

References

[1] El-Mallawany RAH (2002) Tellurite glasses handbook: physical properties and data. CRC Press, Florida, USA

[2] Murawski L, Chung CH, Mackenzie JD (1979) Electrical properties of semiconducting oxide glasses. J Non-Cryst Sol 32:91–104. https://doi.org/10.1016/0022-3093(79)90066-8

[3] Fan J, Zhang Y, Li G, Yue Y (2019) Tellurium nanoparticles enhanced electrochemical performances of TeO_2–V_2O_5–Al_2O_3 glass anode for lithium-ion batteries. J Non-Cryst Sol 521:119491. https://doi.org/10.1016/j.jnoncrysol.2019.119491

[4] Chung CH (1979) Electrical properties of semiconducting oxide glasses based on vanadium oxide. PhD Dissertation University of California

[5] Okoczuk P, Wójcik NA, Murawski L, Wicikowski L, Łapiński M, Winiarz P, Kościelska B (2023) Increasing the conductivity of V_2O_5–TeO_2 glass by crystallization: structure and charge transfer studies. J Mater Sci. https://doi.org/10.1007/s10853-023-08560-x

[6] Pietrzak TK, Wasiucionek M, Garbarczyk JE (2021) Towards higher electric conductivity and wider phase stability range via nanostructured glass-ceramics processing. Nanomaterials 11(5):1321. https://doi.org/10.3390/nano11051321

[7] Pietrzak TK, Pawliszak Ł, Michalski PP, Wasiucionek M, Garbarczyk JE (2014) Highly conductive $90V_2O_5{\cdot}10P_2O_5$ nanocrystalline cathode materials for lithium-ion batteries. Procedia Eng 98:28–35. https://doi.org/10.1016/j.proeng.2014.12.483

[8] Garbarczyk JE, Pietrzak TK, Wasiucionek M, Kaleta A, Dorau A, Nowiński J (2015) High electronic conductivity in nanostructured materials based on lithium-iron-vanadate-phosphate glasses. Sol State Ion 272:53–59. https://doi.org/10.1016/j.ssi.2014.12.019

[9] Pietrzak TK, Michalski PP, Kruk PE, Ślubowska W, Szlachta K, Duda P, Nowiński J, Wasiucionek M, Garbarczyk JE (2017) Nature of electronic conductivity in olivine-like glasses and nanomaterials of Li_2O–FeO–V_2O_5–P_2O_5 system. Sol State Ion 302:45–48. https://doi.org/10.1016/j.ssi.2016.11.031

[10] Nowagiel M, Hul A, Kazakevicius E, Kežionic A, Garbarczyk JE, Pietrzak T (2023) Optimization of electrical properties of nanocrystallized $Na_3M_2(PO_4)_2F_3$ NASICON-like glasses (M = V, Ti, Fe). Coatings 13:482. https://doi.org/10.3390/coatings13030482

[11] Kościelska B, Murawski L, Chudinov S, Stizza S (1999) Hopping conduction in glassy and crystallized Bi–Sr–Ca–Cu–O system. Phys State Sol B Basic Res 211:751–757. https://doi.org/10.1002/(SICI)1521-3951(199902)211:2%3c751::AID-PSSB751%3e3.0.CO;2-Q

[12] Murawski L, Kościelska B, Barczyński RJ, Gazda M, Kusz B, Andrzejewski B, Stizza S, Chudinov S (2000) The electronic conductivity mechanism in Bi–Sr–Ca–Cu–O glass-ceramics. Philosophi Mag B 80:1093–1103. https://doi.org/10.1080/01418630008221976

[13] Reich KV, Shklovskii BI (2016) Dielectric constant and charging energy in array of touching nanocrystals. Appl Phys Lett 108:11. https://doi.org/10.1063/1.4944407

[14] Fu H, Reich KV, Shklovskii BI (2016) Hopping conductivity and insulator-metal transition in films of touching semiconductor nanocrystals. Phys Rev B 93:125430. https://doi.org/10.1103/PhysRevB.93.125430

[15] Avrami M (1939) Kinetics of phase change. I: general theory. J Chem Phys 7:1103–1112. https://doi.org/10.1063/1.1750380

[16] Avrami M (1940) Kinetics of phase change. II Transformation-time relations for random distribution of nuclei. J Chem Phys 8:212–224. https://doi.org/10.1063/1.1750631

[17] Avrami M (1941) Granulation, phase change, and microstructure kinetics of phase change. III J Chem Phys 9:177–184. https://doi.org/10.1063/1.1750872

[18] Ho Lam RS, Rogers MA (2011) Experimental validation of the modified Avrami model for non-isothermal crystallization conditions. Cryst Eng Comm 13:866–875. https://doi.org/10.1039/c0ce00523a

[19] Wang Q, Sun T, Zheng S, Li L, Ma T, Liang J (2021) A new tunnel-type V_4O_9 cathode for high power density aqueous zinc ion batteries. Inorg Chem Front 8:4497–4506

[20] Jayasinghe GDLK, Dissanayake MAKL, Careema MA, Souquet JL (1997) Electronic to ionic conductivity of glasses in the Na_2O–V_2O_5–TeO_2 system. Sol State Ion 93:291–295

[21] Zhang Y, Wang P, Li G, Fan J, Gao C, Wang Z, Yue Y (2019) Clarifying the charging induced nucleation in glass anode of Li-ion batteries and its enhanced performances. Nano Energy 57:592–599. https://doi.org/10.1016/j.nanoen.2018.12.088

[22] Zhang Y, Wang P, Zheng T, Li D, Li G, Yue Y (2018) Enhancing Li-ion battery anode performances via disorder/order engineering. Nano Energy 49:596–602. https://doi.org/10.1016/j.nanoen.2018.05.018

[23] Shelby JE (2005) Introduction to glass science and technology, 2nd edn. The Royal Society of Chemistry, Cambrige, UK

[24] Pietrzak TK, Wasiucionek M, Nowiński JL, Garbarczyk JE (2013) Isothermal nanocrystallization of vanadate–phosphate glasses. Sol State Ion 251:78–82. https://doi.org/10.1016/j.ssi.2013.01.004

[25] Sun NX, Liu XD, Lu K (1996) An explanation to the anomalous avrami exponent. Scr Mater 34(8):1201–1207. https://doi.org/10.1016/1359-6462(95)00657-5

[26] Holder CF, Schaak RE (2019) Tutorial on powder X-ray diffraction for characterizing nanoscale materials. ACS Nano 13:7359–7365. https://doi.org/10.1021/acsnano.9b05157

[27] Ji H, Liu D, Cheng H, Zhang C, Yang L, Ren D (2017) Infrared thermochromic properties of monoclinic VO_2 nanopowders using a malic acid-assisted hydrothermal method for. RSC Adv 7:5189. https://doi.org/10.1039/c6ra26731a

[28] Taleb R, Hadeel R, Thamer SM, Abdullah A, Juzsakova T, Al N (2020) Synthesis, characterization of V_2O_5 nanoparticles and determination of catalase mimetic activity by new colorimetric method. J Therm Anal Calorim 145:297–307. https://doi.org/10.1007/s10973-020-09725-5

[29] Dimitriev Y, Dimitrov V, Arnaudov M, Topalov D (1983) IR-spectral study of vanadate vitreous systems. J Non-Cryst Sol 57:147–156. https://doi.org/10.1016/0022-3093(83)90417-9

[30] Abd El-Moneim A (2002) DTA and IR absorption spectra of vanadium tellurite glasses. Mater Chem Phys 73:318–322. https://doi.org/10.1016/S0254-0584(01)00355-8

[31] Kjeldsen J, Yue Y, Bragatto CB, Rodrigues ACM (2013) Electronic conductivity of vanadium-tellurite glass-ceramics. J Non-Cryst Solids 378:196–200. https://doi.org/10.1016/j.jnoncrysol.2013.07.011

[32] Kjeldsen J, Rodrigues ACM, Mossin S, Yue Y (2014) Critical V_2O_5/TeO_2 ratio inducing abrupt property changes in vanadium tellurite glasses. J Phys Chem B 118:14942–14948. https://doi.org/10.1021/jp508910m

[33] Ioffe VA, Patrina IB (1970) Comparison of the small-polaron theory with the experimental data of current transport in V_2O_5. Phys State Sol (B) 40:389–395. https://doi.org/10.1002/pssb.19700400140

[34] Mott NF (1968) Conduction in glasses containing transition metal ions. J Non-Cryst Sol 1:1–17. https://doi.org/10.1016/0022-3093(68)90002-1

[35] Szymanski NJ, Liu ZTY, Alderson T, Podraza N, Sarin P, Khare S (2018) Electronic and optical properties of vanadium oxides from first principles. Comput Mater Sci 146:310–318. https://doi.org/10.1016/j.commatsci.2018.01.048

[36] Kosuge K, Kachi S (1965) Phase transition in V_6O_{13}. J phys soc Jpn 20:178–179. https://doi.org/10.1143/JPSJ.20.178

[37] Ghosh A (1989) Temperature-dependent thermoelectric power of semiconducting bismuth-vanadate glass. J Appl Phys 65:227. https://doi.org/10.1063/1.342575

[38] Mansingh A, Dhawan A (1978) Thermoelectric power in transition metal alloys. J Phys C: Sol State Phys 11:3439–3445. https://doi.org/10.1088/0022-3719/11/16/013

[39] Flynn BW (1977) Electrical and optical properties of vanadium tellurite glasses. PhD Dissertation The University of Edinburg

[40] Murawski L, Sanchez C, Livage J, Audiere JP (1990) Small polaron transport in amorphous V_2O_5 films. J Non-Cryst Sol 124:71–75. https://doi.org/10.1016/0022-3093(90)91081-2

[41] Murawski L (1993) Electronic conductivity in oxide glasses. Polish Ceram Bull 5:111–122